

InstantSplat: Unbounded Sparse-view Pose-free Gaussian Splatting in 40 Seconds

Zhiwen Fan^{*†1,2}, Wenyan Cong^{*1}, Kairun Wen^{*3}, Kevin Wang¹, Jian Zhang³, Xinghao Ding³,
Danfei Xu^{2,4}, Boris Ivanovic², Marco Pavone^{2,5}, Georgios Pavlakos¹, Zhangyang Wang¹, Yue Wang^{2,6}

* Equal contribution † Project leader

¹University of Texas at Austin ²Nvidia Research
³Xiamen University ⁴Georgia Institute of Technology
⁵Stanford University ⁶University of Southern California



Figure 1. **Novel View Synthesis Comparisons (Sparse-View, Pose-Free).** We introduce InstantSplat, an efficient framework for simultaneous pose estimation and novel view synthesis in unrestricted scenarios. This approach incorporates 3D priors derived from a dense stereo model, a streamlined framework capable of reconstructing 3D scenes and enabling view synthesis within one minute, for large-scale scenes. Moreover, our method markedly enhances both pose estimation accuracy and rendering quality.

Abstract

While novel view synthesis (NVS) has made substantial progress in 3D computer vision, it typically requires an initial estimation of camera intrinsics and extrinsics from dense viewpoints. This pre-processing is usually conducted via a Structure-from-Motion (SfM) pipeline, a procedure that can be slow and unreliable, particularly in sparse-view scenarios with insufficient matched features for accurate reconstruction. In this work, we integrate the strengths of point-based representations (e.g., 3D Gaussian Splatting, 3D-GS) with end-to-end dense stereo models (DUST3R) to tackle the complex yet unresolved issues in NVS under unconstrained settings, which encompasses pose-free and sparse view challenges. Our framework, **InstantSplat**, unifies dense stereo priors with 3D-GS to build 3D Gaussians of large-scale scenes from sparse-

view & pose-free images in less than 1 minute. Specifically, InstantSplat comprises a Coarse Geometric Initialization (CGI) module that swiftly establishes a preliminary scene structure and camera parameters across all training views, utilizing globally-aligned 3D point maps derived from a pre-trained dense stereo pipeline. This is followed by the Fast 3D-Gaussian Optimization (F-3DGO) module, which jointly optimizes the 3D Gaussian attributes and the initialized poses with pose regularization. Experiments conducted on the large-scale outdoor Tanks & Temples datasets demonstrate that InstantSplat significantly improves SSIM (by 32%) while concurrently reducing Absolute Trajectory Error (ATE) by 80%. These establish InstantSplat as a viable solution for scenarios involving pose-free and sparse-view conditions. Project page: <https://instantsplat.github.io/>.

1. Introduction

Novel-view synthesis (NVS) has been a long standing goal in computer vision, involving rendering observations from unseen viewpoints of a scene based on a specific set of input images. Capturing viewpoints in a “casual” manner, especially with a limited number of shots (a.k.a. sparse-view) using a smartphone in an uncontrolled environment, is pivotal for scaling up 3D content creation, digital twin construction, and augmented reality applications.

Although recent advancements [11, 20, 30, 38] have shown notable progress in sparse-view synthesis (SVS), a detailed analysis uncovers a significant challenge yet to be solved: The sparse input data collected does not sufficiently cover the scene, preventing Structure from Motion (SfM) pipelines like COLMAP [24] from estimating accurate camera parameters. Previous research in SVS [11, 20] typically assumes precise camera poses even in sparse-view scenarios by leveraging all dense views for pre-computation, an assumption that is rarely valid. On the other hand, another line of research explores pose-free settings using techniques such as Neural Radiance Field (NeRF) or 3D Gaussian Splatting (3D-GS), exemplified by Nope-NeRF [5] and CF-3DGS [10]. These approaches presume dense data coverage (often from video sequences), an assumption that may not be viable in “casual” scenarios. Additionally, all previous methods assume known camera intrinsics prior to the reconstruction stage, adding an extra layer of complexity in real-world applications where such information may not be readily available.

In this paper, we introduce a holistic solution to unconstrained sparse-view synthesis that obviates the need for pre-computed camera intrinsics and extrinsics. We present InstantSplat, a framework that unifies the explicit 3D Gaussian representation with pose priors obtained from an end-to-end dense stereo model—DUST3R [31]. DUEs3R facilitates the acquisition of initial scene geometry from predicted and globally aligned point maps of sparse views and enables efficient camera information and pose retrieval. Following this, 3D Gaussians are established atop the globally aligned yet coarse geometry, promoting the concurrent optimization of 3D Gaussian attributes and camera parameters. By imposing additional constraints on camera parameters and merely adjusting Gaussian attributes—eschewing complex adaptive density control—the reconstruction process for large-scale scenes can be completed in under *one minute* on a modern GPU (Nvidia A100). Our experiments are conducted on two large-scale outdoor datasets: Tanks & Temples [14] and MVIImgNet [40], featuring sampled sparse views. Our evaluations, focusing on view synthesis quality and camera pose accuracy, demonstrate that our method remarkably surpasses previous pose-free methods. Notably, InstantSplat increases the SSIM from 0.68 to 0.89, a 32% improvement, and reduces the ATE from

0.055 to 0.011, while significantly accelerating the optimization (from ~ 2 hours to approximately 1 minute) than Nope-NeRF [5].

2. Related Works

3D Representations for NVS. Novel view synthesis aims to generate unseen views of an object or scene from a given set of images [1, 18]. Neural Radiance Fields (NeRF)[19], one of the most prominent methods in recent years, employs Multilayer Perceptrons (MLPs) to represent 3D scenes, taking the directions and positions of 3D points as input and employing volume rendering for image synthesis. Despite its popularity, NeRF faces challenges in terms of speed during both training and inference phases. Subsequent enhancements primarily focus on either enhancing quality[2–4] or improving efficiency [21, 25–27], with few achieving both. Recent advancements in unstructured radiance fields[7, 13, 37] introduce a set of primitives to represent scenes. Notably, 3D Gaussian Splatting[13] uses anisotropic 3D Gaussians [43] to depict radiance fields, coupled with differentiable splatting for rendering. This method has shown considerable success in rapidly reconstructing complex real-world scenes with high quality, particularly excelling in capturing high-frequency details.

Unconstraint Novel View Synthesis. Neural radiance fields (NeRFs) or 3D Gaussian Splatting traditionally require over a hundred images as input and utilize preprocessing software, such as COLMAP [24], to compute camera intrinsics and extrinsics. The dense coverage of the capture images is essential for reconstructing the details of a 3D scene but significantly limits practical applications. To address the challenge of the requisite number of views, various studies have introduced different regularization techniques to optimize the radiance fields. For instance, Depth-NeRF [9] employs additional depth supervision to enhance rendering quality. RegNeRF [20] introduces a depth smoothness loss for geometric regularization, aiding in stabilizing training. DietNeRF [11] and SinNeRF [36] leverages supervision in the CLIP/DINO-ViT embedding space [6, 23] to constrain the rendering of unseen views. PixelNeRF [39] utilizes a convolutional encoder to gather context information, enabling the prediction of 3D representations from sparse inputs. More recent efforts, like FreeNeRF [38], introduce a dynamic frequency control module for few-shot NeRF, while SparseNeRF [30] presents a novel spatial continuity loss that leverages monocular depth estimators to enhance spatial coherence. Concurrently, ReconFusion [34], FSGS [42], and SparseGS [35] employ monocular depth estimators or diffusion models with additional synthesized views for optimizing 3D representations. However, these methods require known ground-truth camera poses, a challenging prerequisite as the commonly used Structure-from-Motion (SfM)

algorithms often fail with sparse inputs due to insufficient image correspondences. Another line of research focuses on pose-independent 3D optimization. NeRFmm [33] simultaneously optimizes camera intrinsics, extrinsics, and NeRF training. BARF [16] introduces a coarse-to-fine strategy for encoding camera poses and joint NeRF optimization. SCNeRF [12] adds camera distortion parameterization and employs geometric loss for ray regularization. Similarly, GARF [12] demonstrates that Gaussian-MLPs facilitate more straightforward and accurate joint optimization of pose and scene. SPARF [28] adds Gaussian noise to simulate noisy camera poses. Recent works, such as NopeNeRF [5], Lu-NeRF [8], LocalRF [17] and CF-3DGS [10], leverage depth information to constrain NeRF or 3DGS optimization, yet these pose-independent approaches generally presume the input are dense video sequences with known camera intrinsics, which are not always viable in practical cases.

Considering the aforementioned factors, particularly in the context of sparse-view conditions, it becomes imperative for research to progress toward situations where camera poses and intrinsics are unknown. Commonly, under such sparse conditions, the COLMAP software tends to be unreliable to produce camera poses and register all the input images. This necessitates a different approach: optimizing a 3D representation with sparse input views where both camera poses and intrinsics are unknown, compelling a paradigm shift in research to address these uncertainties.

Effective Priors for View Synthesis. Current methodologies often depend on offline software (COLMAP) to pre-compute camera poses, which also yields a sparse point cloud as a byproduct. Depth-NeRF [9] and 3D-GS [13] advocate for leveraging this point cloud as a form of effective supervision and as initial conditions for optimization. To address the lack of camera poses or dense camera views, the integration of monocular depth priors is extensively employed in 3D optimization efforts [5, 10, 30, 35, 42]. Additionally, image matching techniques have been investigated to identify additional cross-view pixel correspondences, facilitating the training process [15, 28].

While these methods are beneficial, the approach of pre-computing camera extrinsics from densely sampled viewpoints and employing near-perfect camera poses for initialization is not always viable in practical sparse-view scenarios. In response, we introduce a unified framework that incorporates explicit point-based representations alongside the cutting-edge end-to-end dense stereo network, DUST3R [31]. This approach eliminates the need for sparse-view camera pose estimation and the presumption that camera poses are unknown beforehand. By initializing the scene geometry through inferences made by the stereo model, —which is markedly faster than COLMAP— we can deduce camera poses and intrinsics from the established point

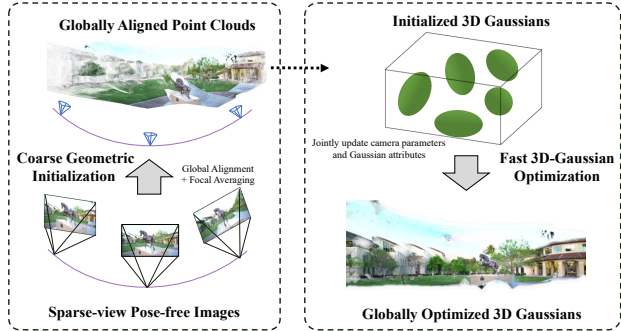


Figure 2. **Overall Framework of InstantSplat.** Starting with sparse, unposed images, the Coarse Geometric Initialization (left) rapidly predicts global aligned point clouds and initializes poses (20.6 seconds). Subsequently, the Fast 3D-Gaussian Optimization (right) leverages this robust initialization to conduct streamlined optimizations of 3D Gaussians and camera parameters (16.67 seconds).

cloud, thereby facilitating the training of 3D-GS.

3. Preliminary

3.1. 3D Gaussian Splatting

3D Gaussian Splatting (3D-GS) [13] is an explicit 3D scene representation utilizing a set of 3D Gaussians to model the scene. A 3D Gaussian is parameterized by a mean vector $\mathbf{x} \in \mathbb{R}^3$ and a covariance matrix $\Sigma \in \mathbb{R}^{3 \times 3}$:

$$G(\mathbf{p}) = \frac{1}{(2\pi)^{3/2} |\Sigma|^{1/2}} e^{-\frac{1}{2}(\mathbf{p}-\mathbf{x})^T \Sigma^{-1}(\mathbf{p}-\mathbf{x})} \quad (1)$$

To represent the view-direction-dependent, spherical harmonic (SH) coefficients are attached to each Gaussian, and the color is computed via $\mathbf{c}(\mathbf{d}) = \sum_{i=1}^n \mathbf{c}_i \mathcal{B}_i(\mathbf{d})$, where \mathcal{B}_i is the i^{th} SH basis. And the color is rendered via $\mathbf{c} = \sum_{i=1}^n \mathbf{c}_i \alpha_i \prod_{j=1}^{i-1} (1 - \alpha_j)$,

where \mathbf{c}_i is the color computed from the SH coefficients of the i^{th} Gaussian. α_i is given by evaluating a 2D Gaussian with covariance multiplied by a learned per-Gaussian opacity. The 2D covariance matrix is calculated by projecting the 3D covariance to the camera coordinates. The 3D covariance matrix is decomposed into a scaling matrix and a rotation matrix and are optimized as Gaussian attributes.

In summary, 3D-GS uses a set of 3D Gaussians $\{\mathcal{S}_i | i = 1, 2, \dots, n\}$ to represent and render a scene, where each 3D Gaussian \mathcal{S} is characterized by: position $\mathbf{x} \in \mathbb{R}^3$, a series of SH coefficients $\{\mathbf{c}_i \in \mathbb{R}^3 | i = 1, 2, \dots, n\}$, opacity $\alpha \in \mathbb{R}$, rotation $\mathbf{q} \in \mathbb{H}$ and scaling $\mathbf{s} \in \mathbb{R}^3$.

3.2. End-to-end Dense Stereo Model: DUST3R

A traditional dense 3D reconstruction stereo pipeline is meticulously designed to transform stereo or multiple images into an intricate 3D model (e.g., depth map) of a

scene. The process commences with the acquisition of input images, denoted as $\{(\mathbf{I}_i \in \mathbb{R}^{H \times W \times 3})\}_{i=1}^N$. Initially, Structure-from-Motion (SfM) techniques are employed to ascertain the camera extrinsics $\{\mathbf{T}_i \in \mathbb{R}^{3 \times 4}\}_{i=1}^N$ and intrinsics $\{\mathbf{K}_i \in \mathbb{R}^{3 \times 3}\}_{i=1}^N$. Utilizing COLMAP, feature detection, and extraction are performed for each image, predicated on the assumption that the images exhibit good texture, consistent illumination, and significant visual overlap. Subsequently, feature matching and geometric verification are conducted to establish robust correspondences across multiple image pairs. The process of incremental reconstruction involves registering high-confidence images, utilizing triangulation and bundle adjustment to refine camera extrinsics and generate a sparse point cloud of the scene. Dense reconstruction, particularly through Multi-View Stereo (MVS), is then applied to extract more detailed scene geometry, resulting in pixel-level depth maps for further applications.

However, segmenting the contemporary SfM and MVS pipeline into a series of isolated minimal problems may introduce noise and escalate the complexity and engineering effort required for the pipeline’s holistic functionality. The new DUST3R model [31] aims to integrate the SfM and MVS processes, estimating point maps $\{(\mathbf{P}_i \in \mathbb{R}^{H \times W \times 3})\}_{i=1}^N$ and confidence maps $\{(\mathbf{O}_i \in \mathbb{R}^{H \times W})\}_{i=1}^N$ directly from uncalibrated and unposed cameras ($\{(\mathbf{I}_i \in \mathbb{R}^{H \times W \times 3})\}_{i=1}^N$). This end-to-end approach posits that each sub-problem should synergize within a singular framework, where dense reconstruction benefits from the sparse scene generated for camera pose recovery, and vice versa, thus fostering a more efficient and coherent 3D reconstruction process. Specifically, the training objective of DUST3R is based on regression of the unprojected and normalized point maps of two input views. Here, the ground-truth pointmaps from the datasets are as $\hat{\mathbf{P}}_{1,1}$ and $\hat{\mathbf{P}}_{2,1}$, obtained from along with two corresponding views $\{1, 2\}$ where the camera origin as view 1, on which the ground-truth is defined. In this context, the subscript $\{2, 1\}$ in $\hat{\mathbf{P}}_{2,1}$ signifies that the origin of the coordinate system for view 2 is anchored at view 1. The regression loss for training DUST3R is as

$$\mathcal{L} = \left\| \frac{1}{z_i} \cdot \mathbf{P}_{v,1} - \frac{1}{\hat{z}_i} \cdot \hat{\mathbf{P}}_{v,1} \right\|. \quad (2)$$

where view $v \in \{1, 2\}$, \mathbf{P} and $\hat{\mathbf{P}}$ are the prediction and ground-truth, separately. To handle the scale ambiguity between prediction and ground-truth, DUST3R normalizes the predicted and ground-truth pointmaps by scaling factors $z_i = \text{norm}(\mathbf{P}_{1,1}, \mathbf{P}_{2,1})$ and $\hat{z}_i = \text{norm}(\hat{\mathbf{P}}_{1,1}, \hat{\mathbf{P}}_{2,1})$, respectively, which simply represent the average distance, noted as symbol \mathbf{D} of all valid points to the origin:

$$\text{norm}(\mathbf{P}_{1,1}, \mathbf{P}_{2,1}) = \frac{1}{|\mathbf{D}_1| + |\mathbf{D}_2|} \sum_{v \in \{1,2\}} \sum_{i \in \mathbf{D}_v} \|\mathbf{P}_v^i\|. \quad (3)$$

4. Method

Overview In this section, we introduce a new pipeline that incorporates DUST3R as a 3D prior model, providing globally aligned initial scene geometry for 3D Gaussians. This allows for the subsequent calculation of camera poses and intrinsics from the dense point maps, which are then jointly optimized with all other 3D Gaussian attributes. The supervision signals are derived backward from the photometric discrepancies between the rendered images via splatting and the ground-truth images. An illustrative overview of our method is depicted in Fig. 2.

4.1. Coarse Geometric Initialization

3D dense prior network, DUST3R, accepts only two images as input and generates per-pixel pointmap and confidence maps as outputs. A very efficient post-processing optimization can be leveraged to solve the per-view pixel-to-3D mapping and the incremental relative poses, which we will detail later.

Recovering Camera Intrinsics. We can have the 1:1 mapping from the pixel lattice to pointmap where we can build the mapping from 2D to the camera coordinate system. We can first solve the simple optimization based on Weiszfeld algorithm [22] to calculate per-camera focal:

$$f^* = \arg \min_f \sum_{i=0}^W \sum_{j=0}^H \mathbf{O}^{i,j} \left\| (i', j') - f \frac{(\mathbf{P}^{i,j,0}, \mathbf{P}^{i,j,1})}{\mathbf{P}^{i,j,2}} \right\|,$$

where $i' = i - \frac{W}{2}$ and $j' = j - \frac{H}{2}$ denote centered pixel indices. Assuming a single-camera setup akin to COLMAP’s methodology, we average the focal length calculations to obtain a robust estimate: $\bar{f} = \frac{1}{N} \sum_{i=1}^N f_i^*$. The resulting \bar{f} represents the computed focal length that is utilized in subsequent processes.

Pair-wise to Globally Aligned Poses. DUST3R only takes image pairs as inputs where post-processing is required to align the scale if more than two captures are within the scene. The underlying reason is that the predicted point map are at the normalized scales within its own scale, and such misalignment of each independent calculated relative poses will leads to the scale variance thus, resulting in inaccurate camera poses. Similar to DUST3R we first construct a complete connectivity graph $\mathcal{G}(\mathcal{V}, \mathcal{E})$ of all the N input views, where the vertices \mathcal{V} and each edge $e = (n, m) \in \mathcal{E}$ indicate a shared visual content between images I_n and I_m . To convert the initially predicted point map $\{(\mathbf{P}_i \in \mathbb{R}^{H \times W \times 3})\}_{i=1}^N$ to be globally aligned one $\{(\hat{\mathbf{P}}_i \in \mathbb{R}^{H \times W \times 3})\}_{i=1}^N$, we update the point maps, transformation matrix, and a scale factor: For the complete graph, any image pair $e = (n, m) \in \mathcal{E}$, the point maps $\mathbf{P}_{n,n}, \mathbf{P}_{m,n}$ and confidence maps $\mathbf{O}_{n,n}, \mathbf{O}_{m,n}$. For

clarity, let us define $P_{n,e} := P_{n,n}$, and $P_{m,e} := P_{m,n}$, $O_{n,e} := O_{n,n}$, and $O_{m,e} := O_{m,n}$.

The optimization for the transformation matrix of edge e (T_e), scaling factor σ and point map \tilde{P} are via:

$$\tilde{P}^* = \arg \min_{\tilde{P}, T, \sigma} \sum_{e \in \mathcal{E}} \sum_{v \in e} \sum_{i=1}^{HW} O_{v,e}^i \left\| \tilde{P}_v^i - \sigma_e T_e P_{v,e}^i \right\|. \quad (4)$$

Here, we slightly abuse notation and write $v \in e$ for $v \in \{n, m\}$ if $e = (n, m)$. The idea is that, for a given pair e , the same rigid transformation T_e should align both pointmaps $P_{n,e}$ and $P_{m,e}$ with the world-coordinate pointmaps $\tilde{P}_{n,e}$ and $\tilde{P}_{m,e}$, since $P_{n,e}$ and $P_{m,e}$ are by definition both expressed in the same coordinate frame. To avoid the trivial optimum where $\sigma_e = 0, \forall e \in \mathcal{E}$, we also enforce that $\prod_e \sigma_e = 1$. The benefits of the post-processing to yield a globally aligned point cloud lies in its efficiency where inferring per-view point and confidence maps can be real-time on a modern GPU, and the post-processing for a few images requires only seconds.

4.2. Fast 3D-Gaussian Optimization

3D Gaussian Initializations. The primary objective in 3D-GS optimization, as discussed in [13], is to adeptly refine the set of 3D Gaussians to accurately represent the scene. Traditional initialization with sparse point clouds from Structure from Motion (SfM) provides basic color and positional details. Yet, the inherent sparsity of SfM data demands extensive optimization time to densify, split and refine Gaussians for adequate 3D scene modeling.

In contrast, we advocate for utilizing a globally aligned point map as preliminary scene geometry, replacing the sparse SfM point set for 3D-GS initialization [13]. This approach offers several advantages over sparse SfM point cloud initialization: 1) It addresses the challenging nature of Gaussian parameter optimization, aiming to reconstruct the complete 3D scene and render from any viewpoint, particularly when the training views are significantly below the Nyquist sampling rate. 2) To maintain the optimized 3D Gaussian’s stability and quality, the original authors [13] implemented a complex set of rules to guide the generation of new Gaussians, division of incorrectly optimized Gaussians, and periodic opacity adjustments to eliminate residual Gaussians. Considering these aspects, we leverage a 3D prior model to supply a robust scene structure (a.k.a. globally aligned point maps) with ample primitives to encapsulate the scene’s surfaces. This approach minimizes the need for manual optimization rules (adaptive density control in 3DGS [13]), and thus requiring fewer steps. Specifically, we execute 1k iterations optimization on the initialized 3D Gaussians, omitting the densification, splitting, and opacity reset processes, thereby streamlining and simplifying the optimization procedure.

Jointly Optimizing Poses and Attributes. We observe that aligning camera extrinsics predominantly addresses the issue of inconsistent scale when transitioning from two-view to multi-view scenarios. However, ambiguities arise due to inaccuracies in predicted points or confidence maps, which may be attributed to varying illumination across different views or minor motion blur from handheld capture devices. Consequently, the alignment accuracy is compromised. To mitigate this, we propose a simultaneous optimization of camera extrinsics and a 3D model using a sparse set of training views. We enable the camera parameters to be adjustable alongside the Gaussian attributes. Additionally, we introduce a constraint to ensure that the optimized poses do not deviate excessively from their initial positions. This method aims to refine pose accuracy while maintaining a close adherence to the original extrinsic parameters, thereby enhancing the overall alignment precision in our 3D reconstruction process.

$$S^*, T^* = \arg \min_{S, T} \sum_{v \in N} \sum_{i=1}^{HW} \left\| \tilde{C}_v^i(S, T) - C_v^i(S, T) \right\| + \lambda \cdot \|T - T_0\|.$$

In the given context, the S represents the set of 3D Gaussians, T denotes the camera extrinsics for a specific view, T_0 signifies the initial extrinsics obtained from global alignment, C is the rendering function, and the term λ is introduced to strike a balance between photometric loss and the steps involved in camera optimization. This formulation is pivotal in ensuring that the optimization process is finely tuned to achieve an optimal balance between fidelity to the observed data and adherence to the initial camera poses, facilitating a robust and accurate 3D representation for NVS.

4.3. Aligning Camera Poses on Test Views

In contrast to the conventional approach where exact camera poses for test views are known and typically estimated alongside training views within the same coordinate system (as seen in 3D-GS [13] and NeRF [19]), our scenario involves test views with either unknown or noisy poses. Employing camera poses calculated from DUST3R often results in minor misalignments between predicted and ground-truth images. This necessitates the alignment of camera poses for test views before rendering.

Drawing inspiration from NeRFmm [33], we maintain the 3DGS model trained on training views, in a frozen state while optimizing the camera poses for test views. This optimization process focuses on minimizing the photometric discrepancies between the synthesized images and the actual test views, aiming to achieve a more precise alignment and rendering of the test views for equitable comparisons.

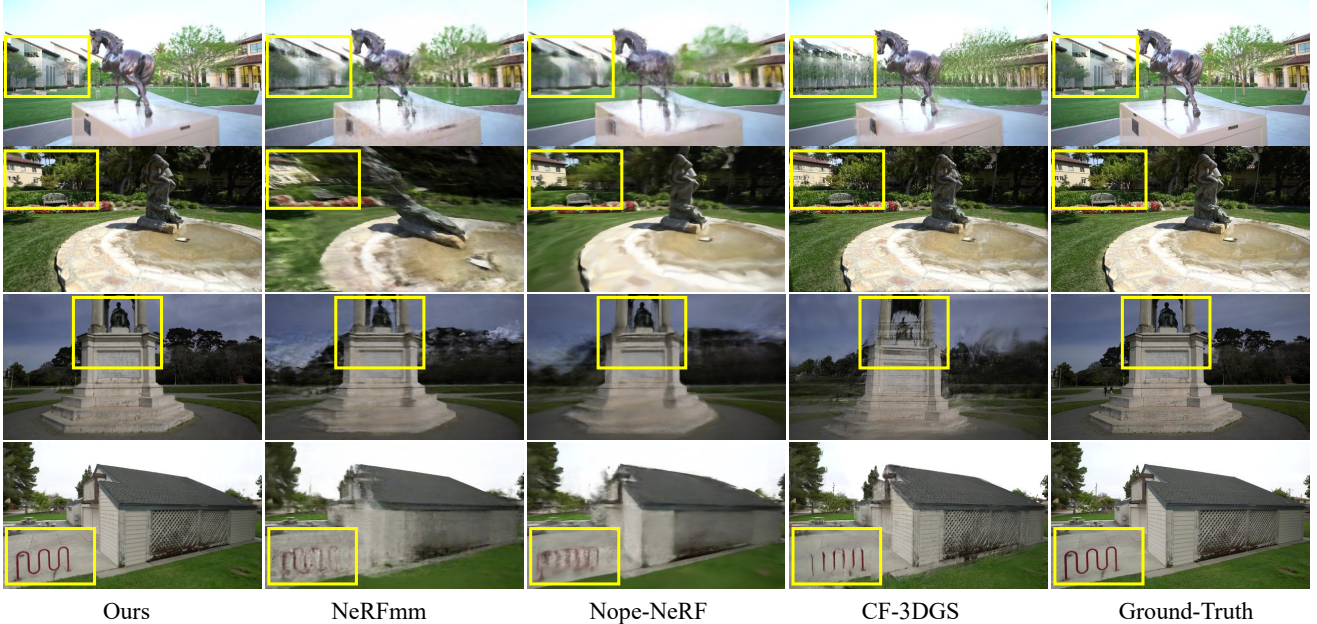


Figure 3. **Visual Comparisons.** We conducted a comparative analysis between InstantSplat and various baseline methodologies. It was noted that InstantSplat adeptly preserves a majority of the scene details, avoiding the artifacts typically induced by inaccurately estimated camera poses, a common issue in CF-3DGS [10]. Moreover, our streamlined framework negates the necessity for strong regularization during training, unlike Nope-NeRF, thereby yielding sharper image details. Additionally, NeRFmm is prone to introducing artifacts during viewpoint transitions, attributable to imprecise joint optimization processes.

Methods	Ours			CF-3DGS			Nope-NeRF			NeRFmm		
	SSIM \uparrow	PSNR \uparrow	LPIPS \downarrow	SSIM \uparrow	PSNR \uparrow	LPIPS \downarrow	SSIM \uparrow	PSNR \uparrow	LPIPS \downarrow	SSIM \uparrow	PSNR \uparrow	LPIPS \downarrow
Barn	0.89	28.94	0.12	0.57	18.29	0.34	0.64	22.48	0.44	0.51	18.28	0.53
Family	0.91	28.69	0.10	0.58	17.06	0.32	0.76	24.82	0.34	0.49	17.74	0.53
Francis	0.90	31.02	0.16	0.63	20.26	0.37	0.65	22.26	0.48	0.61	20.46	0.48
Horse	0.90	28.25	0.10	0.62	17.84	0.32	0.69	21.68	0.39	0.59	18.11	0.45
Ignatius	0.83	26.00	0.16	0.57	18.29	0.34	0.65	24.36	0.41	0.44	19.14	0.50
Avg.	0.89	28.58	0.13	0.59	18.34	0.34	0.68	23.12	0.41	0.53	18.75	0.50

Table 1. **Quantitative Evaluations on the Rendered Tanks and Temples Datasets.** Our method renders significantly clearer details (by LPIPS) compared to other baseline methods, devoid of artifacts typically associated with noisy pose estimation (e.g., CF-3DGS [10], NeRFmm [33]). Furthermore, Nope-NeRF’s regularization approach during training, which involves multiple constraints, restricts the MLPs’ ability to accurately reconstruct scene details. The best results are highlighted in bold.

5. Experiments

5.1. Experimental Setup

Datasets. We conducted comprehensive experiments on real-world datasets featuring large-scale scenes with expansive backgrounds. Specifically, we utilized five scenes from the Tanks and Temples datasets [14], namely Barn, Family, Francis, Horse, and Ignatius. Additionally, we extracted six outdoor scenes from the MVImgNet datasets [40], which include Car, Suv, Bicycle, Chair, Ladder, Bench, and Table. In line with the FSGS protocol [42], we established a sparse-view setting by uniformly selecting 12 views for training and 12 views for evaluation on the Tanks and Temples datasets, with the original number of views ranging from 120 to 200, utilizing approximately 1/10 of the views for training. In a similar vein, we extracted 12 views for both training and evaluation on the MVImgNet

datasets. The camera intrinsics and extrinsics were initially unknown; however, we estimated them and conducted evaluations of pose accuracy on all training samples post Umeyama alignment [29].

Metrics. Our evaluation encompasses two primary tasks: novel view synthesis and camera pose estimation. In the context of camera pose estimation, we present the errors associated with camera rotation and translation, specifically focusing on the Absolute Trajectory Error (ATE) and the Relative Pose Error (RPE), as delineated in [5]. For the task of novel view synthesis, we adopt standard evaluation metrics, namely the Peak Signal-to-Noise Ratio (PSNR), the Structural Similarity Index Measure (SSIM)[32], and the Learned Perceptual Image Patch Similarity (LPIPS)[41].

Baselines. Our evaluation primarily focuses on comparing against pose-free methods. These include Nope-NeRF [5], which utilizes monocular depth maps and

Methods	Ours			CF-3DGS			Nope-NeRF			NeRFmm		
	RPE _t ↓	RPE _r ↓	ATE ↓	RPE _t ↓	RPE _r ↓	ATE ↓	RPE _t ↓	RPE _r ↓	ATE ↓	RPE _t ↓	RPE _r ↓	ATE ↓
Barn	0.189	0.093	0.002	5.391	2.459	0.059	9.051	7.429	0.069	12.410	8.661	0.103
Family	0.414	0.041	0.003	5.803	1.945	0.064	3.663	5.889	0.007	18.178	3.277	0.211
Francis	0.468	0.211	0.004	6.889	3.989	0.094	10.887	4.546	0.147	10.290	5.034	0.222
Horse	0.552	0.037	0.037	10.300	2.307	0.125	16.646	4.102	0.039	16.720	3.258	0.032
Ignatius	0.735	0.168	0.011	0.602	0.174	0.006	11.150	4.550	0.011	17.531	3.275	0.056
Avg.	0.472	0.110	0.011	5.797	2.175	0.070	10.279	5.303	0.055	15.026	4.701	0.125

Table 2. **Quantitative Evaluation of Pose Accuracy on the Tanks and Temples Datasets.** We employ poses derived from COLMAP on full views as the ground-truth reference. The rotational Relative Pose Error (RPE_r) is expressed in degrees, the translational Relative Pose Error (RPE_t) is scaled by 0.01, and the Absolute Trajectory Error (ATE) is quantified using the ground truth scale. The best results are highlighted in bold.

Methods	Ours			CF-3DGS			Nope-NeRF			NeRFmm		
	SSIM ↑	PSNR ↑	LPIPS ↓	SSIM ↑	PSNR ↑	LPIPS ↓	SSIM ↑	PSNR ↑	LPIPS ↓	SSIM ↑	PSNR ↑	LPIPS ↓
Car	0.92	28.91	0.11	0.59	17.85	0.36	0.67	20.63	0.44	0.41	14.68	0.68
Suv	0.89	28.34	0.12	0.60	17.78	0.34	0.66	21.06	0.48	0.42	14.38	0.60
Bicycle	0.75	23.17	0.23	0.23	14.80	0.48	0.29	16.81	0.61	0.13	12.04	0.71
Bench	0.75	23.75	0.23	0.20	15.90	0.47	0.31	18.28	0.58	0.17	13.90	0.67
Chair	0.84	26.54	0.17	0.41	18.10	0.51	0.46	20.42	0.56	0.27	14.53	0.67
Ladder	0.58	20.20	0.29	0.25	15.93	0.48	0.30	17.82	0.64	0.22	15.10	0.66
Table	0.82	25.43	0.17	0.36	16.05	0.52	0.45	18.93	0.56	0.27	12.55	0.67
Avg.	0.79	25.19	0.19	0.38	16.63	0.45	0.45	19.14	0.55	0.27	13.88	0.66

Table 3. **Quantitative Evaluations on the Rendered MVImgNet Datasets.** InstantSplat outperforms baselines in all evaluation metrics.



Figure 4. **Visual Comparisons on the MVImgNet Datasets (Part 1).** We present the rendering results from NeRFmm, Nope-NeRF, CF-3DGS, and ours. The images are arranged from top to bottom, corresponding to the scenes labeled as Car, SUV, Bench, and Bicycle, respectively.

ground-truth camera intrinsics to optimize a neural radiance field. Another method is CF-3DGS [10], which initializes 3D Gaussians from a single view and progressively incorporates all training views, supported by monocular depth maps and ground-truth camera intrinsics. Additionally, we compare with NeRFmm [33], where the joint optimization of NeRF and camera parameters is performed to achieve a plausible solution.

Implementation Details. Our implementation leverages the PyTorch framework, different from 3DGS [13] where we only optimize the 3D Gaussian attributes without im-

plementing adaptive density control. The optimization process is limited to 1,000 iterations, achieving satisfactory results in both rendering quality and pose estimation accuracy. For our model configuration, we employ the DUST3R model [31], trained at a resolution of 512, with a ViT Large encoder and a ViT Base decoder. We set λ as 0.1 during our experiments to constrain the camera poses move to far from the start point. We perform experiments on one Nvidia A100 GPU for fair comparisons.

Methods	Ours			CF-3DGS			Nope-NeRF			NeRFmm		
	RPE _t ↓	RPE _r ↓	ATE ↓	RPE _t ↓	RPE _r ↓	ATE ↓	RPE _t ↓	RPE _r ↓	ATE ↓	RPE _t ↓	RPE _r ↓	ATE ↓
Car	0.145	0.044	0.001	5.734	4.524	0.102	6.986	9.683	0.090	13.706	6.067	0.144
Suv	0.163	0.141	0.002	4.248	3.000	0.031	13.406	10.370	0.190	16.899	7.490	0.164
Bicycle	0.407	0.375	0.006	9.310	9.525	0.149	7.266	15.662	0.116	14.363	13.506	0.066
Bench	0.271	0.244	0.004	7.313	9.618	0.069	14.345	13.699	0.179	13.274	12.429	0.071
Chair	0.386	0.330	0.005	15.430	15.276	0.164	17.447	17.334	0.136	13.449	16.263	0.109
Ladder	0.634	0.603	0.008	11.280	7.883	0.107	18.610	10.557	0.203	15.590	7.770	0.207
Table	0.210	0.214	0.003	17.521	13.757	0.117	9.447	18.595	0.083	17.820	15.443	0.163
Avg.	0.317	0.279	0.004	10.119	9.083	0.106	12.501	13.700	0.142	15.014	11.281	0.132

Table 4. **Quantitative Evaluation of Pose Accuracy on the MVImgNet Datasets.** COLMAP on full views as the ground-truth reference. The rotational Relative Pose Error (RPE_r) is expressed in degrees, the translational Relative Pose Error (RPE_t) is scaled by 0.01, and the Absolute Trajectory Error (ATE) is quantified using the ground truth scale. InstantSplat performs the best in pose estimation.



Figure 5. **Additional Visual Comparisons on the MVImgNet Datasets (Part 2).** We present the rendering results from NeRFmm, Nope-NeRF, CF-3DGS, and ours. The images are arranged from top to bottom, corresponding to the scenes labeled as Chair, Ladder, and Table, respectively.



Figure 6. **Visual Comparisons on MVImgNet.** Rendered images from the “Table” scene are presented alongside visualizations of the learned camera trajectories. Our results exhibit sharper details and predominantly aligned pose estimations.

5.2. Experimental Results

Quantitative and Qualitative Results We assessed the performance of several methods in novel view synthesis and pose estimation on Tanks and Temples datasets, summarizing their quantitative metrics in Tab. 1 and Tab. 2. The methods include the Gaussian Splatting-based CF-3DGS [10] and NeRF-based methods like Nope-NeRF [5] and NeRFmm [33]. In the Tanks and Temples dataset, Nope-NeRF utilizes MLPs and achieves notable accuracy in rendering quality and pose estimation. However, it tends to produce overly blurred renderings due to the heavy constraints from its geometric field and demonstrates slow training (~ 2 hours) and inference speeds (~ 30 seconds for one frame), which may hinder its practical application. CF-3DGS, employing Gaussian Splatting, delivers good rendering quality but is prone to artifacts when changing viewpoints, a consequence of the complex optimization process with erroneous pose predictions, as evidenced in Fig. 3. CF-3DGS requires more complex optimization, incorporating both local and global optimization stages, along with adaptive density control and opacity reset policies. Both Nope-NeRF and CF-3DGS presuppose known focal lengths, which restricts their broader utility. NeRFmm, aiming to optimize camera parameters and the radiance field concurrently, tends to yield suboptimal results due to the challenges of naive joint optimization. While the baselines demonstrate reasonable performance in sparse-view rendering, the pose metrics reveal artifacts attributable to sparse observations and inaccurately estimated poses. Similar observations can be seen in the experiments conducted on MVImgNet datasets, as is shown in Fig. 4, Fig. 5, Tab. 3, Tab. 4 and Fig. 6. This is especially problematic for CF-3DGS and Nope-NeRF, which require dense video sequences, akin to SLAM, and thus struggle with sparse-view scenarios. Conversely, our method, initializes with a coarse scene geometry and globally aligned camera parameters, employs a rapid 3D Gaussian optimization process, offering a more streamlined and efficient solution. Our holistic pipeline requires less than 1 minute for initialization and optimization, benefiting from the integration of end-to-end

Scenes	No Averaging Focal				Full Model (InstantSplat)			
	PSNR \uparrow	SSIM \uparrow	RPE $_t$ \downarrow	RPE $_r$ \downarrow	PSNR \uparrow	SSIM \uparrow	RPE $_t$ \downarrow	RPE $_r$ \downarrow
Barn	26.38	0.8356	0.495	0.167	28.94	0.8905	0.189	0.093
Family	28.12	0.8998	0.538	0.051	28.69	0.9076	0.414	0.041
Francis	29.99	0.8864	0.778	0.213	31.02	0.9016	0.468	0.211
Horse	27.15	0.8811	2.516	0.061	28.25	0.9045	0.552	0.037
Ignatius	24.24	0.7729	0.939	0.182	26.00	0.8305	0.735	0.168
Avg.	27.18	0.8552	1.053	0.135	28.58	0.8900	0.472	0.110

Table 5. **Ablation Study on the Impact of Averaging Focal Length.** Utilizing the averaged focal length for subsequent global alignment and 3D Gaussian joint optimization enhances both the rendering quality and the accuracy of the final pose estimation.

Scenes	No Joint Optimization				Full Model (InstantSplat)			
	PSNR \uparrow	SSIM \uparrow	RPE $_t$ \downarrow	RPE $_r$ \downarrow	PSNR \uparrow	SSIM \uparrow	RPE $_t$ \downarrow	RPE $_r$ \downarrow
Barn	26.56	0.8530	0.382	0.231	28.94	0.8905	0.189	0.093
Family	27.81	0.9017	0.451	0.061	28.69	0.9076	0.414	0.041
Francis	29.74	0.8952	0.405	0.224	31.02	0.9016	0.468	0.211
Horse	26.59	0.8827	1.127	0.106	28.25	0.9045	0.552	0.037
Ignatius	23.41	0.7408	1.020	0.245	26.00	0.8305	0.735	0.168
Avg.	26.82	0.8547	0.677	0.173	28.58	0.8900	0.472	0.110

Table 6. **Ablation Study on the Effect of Joint Optimization.** Concurrently updating the camera extrinsics and Gaussian attributes markedly enhances the rendering quality.

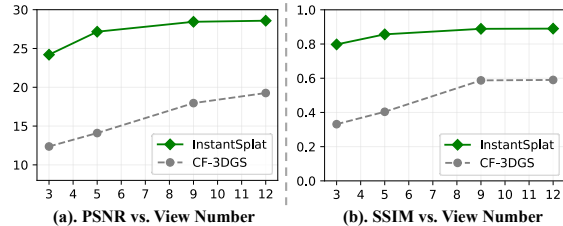


Figure 7. **Ablation on Training View Number.** We study the impact of the training view number to the rendering quality. Comparisons are between our model and CF-3DGS, on the Tanks and Temples datasets

dense stereo priors and the streamlined 3D Gaussian optimization process.

5.3. Ablation Studies

Effect of Averaging Focal Length. Experiments indicate that independent calculation of camera focal length results in a diversity of outcomes, adversely affecting rendering quality and pose estimation accuracy, as evidenced in Tab. 5. The core issue stems from the coupling of a focal length with globally aligned camera extrinsics, which leads to suboptimal pose estimation. This scenario complicates the 3D Gaussian optimization process, impacting the overall performance.

Effect of Joint Optimization. The globally alignment algorithm does not yield pixel-wise accurate extrinsics, primarily due to the resolution loss from the resizing operation on the point map, and the artifacts in the capturing process. We analyzed the effects of updating Gaussian attributes independently (referenced on the left in Tab. 6) versus jointly optimizing camera extrinsics and Gaussian attributes (referenced on the right in Tab. 6). It is evident that further refinement of camera extrinsics can steer the 3D Gaussians

towards a more accurate solution, thereby enhancing the sharpness and detail in the resulting images.

Effect of View Number and Efficiency Analysis. We conduct experiments with varying numbers of training views to assess the model’s generalization capabilities. As illustrated in Fig 7, InstantSplat consistently outperforms CF-3DGS [10], another 3D Gaussian-based pose-free framework. Furthermore, we analyze the time consumption for each module within our framework. Specifically, for 12 training views, it takes 20.6 seconds to acquire the coarse geometry from a pre-trained dense stereo model, while the fast 3D Gaussian Optimization requires 16.67 seconds for 1000 iterations.

6. Conclusion

We introduced InstantSplat, designed to reconstruct scene efficiently from sparse-view unposed images. Our approach leverages dense stereo priors for coarse scene initialization, offering preliminary estimates of the 3D geometry and camera parameters. To further refine these scene attributes and camera parameters, a rapid 3D Gaussian Optimization strategy that jointly optimizes the 3D Gaussian attributes and camera extrinsics. This results in an efficient pipeline capable of reconstructing the 3D scene from unposed images in under one minute. Significantly, our method demonstrates superior rendering quality and pose estimation accuracy compared to existing methodologies, underscoring its effectiveness in handling sparse-view data.

References

- [1] Shai Avidan and Amnon Shashua. Novel view synthesis in tensor space. In *Proceedings of IEEE Computer Society Conference on Computer Vision and Pattern Recognition*, pages 1034–1040. IEEE, 1997. 2
- [2] Jonathan T. Barron, Ben Mildenhall, Dor Verbin, Pratul P. Srinivasan, and Peter Hedman. Mip-NeRF 360: Unbounded Anti-Aliased Neural Radiance Fields. *2022 IEEE/CVF Conference on Computer Vision and Pattern Recognition (CVPR)*, pages 5460–5469, 2022. 2
- [3] Jonathan T Barron, Ben Mildenhall, Dor Verbin, Pratul P Srinivasan, and Peter Hedman. Mip-nerf 360: Unbounded anti-aliased neural radiance fields. In *Proceedings of the IEEE/CVF Conference on Computer Vision and Pattern Recognition*, pages 5470–5479, 2022.
- [4] Jonathan T Barron, Ben Mildenhall, Dor Verbin, Pratul P Srinivasan, and Peter Hedman. Zip-nerf: Anti-aliased grid-based neural radiance fields. In *Proceedings of the IEEE/CVF International Conference on Computer Vision*, pages 19697–19705, 2023. 2
- [5] Wenjing Bian, Zirui Wang, Kejie Li, Jia-Wang Bian, and Victor Adrian Prisacariu. Nope-nerf: Optimising neural radiance field with no pose prior. In *Proceedings of the IEEE/CVF Conference on Computer Vision and Pattern Recognition*, pages 4160–4169, 2023. 2, 3, 6, 9
- [6] Mathilde Caron, Hugo Touvron, Ishan Misra, Hervé Jégou, Julien Mairal, Piotr Bojanowski, and Armand Joulin. Emerging properties in self-supervised vision transformers. In *Proceedings of the IEEE/CVF international conference on computer vision*, pages 9650–9660, 2021. 2
- [7] Zhang Chen, Zhong Li, Liangchen Song, Lele Chen, Jingyi Yu, Junsong Yuan, and Yi Xu. Neurf: A neural fields representation with adaptive radial basis functions. In *Proceedings of the IEEE/CVF International Conference on Computer Vision*, pages 4182–4194, 2023. 2
- [8] Zezhou Cheng, Carlos Esteves, Varun Jampani, Abhishek Kar, Subhransu Maji, and Ameesh Makadia. Lu-nerf: Scene and pose estimation by synchronizing local unposed nerfs. In *Proceedings of the IEEE/CVF International Conference on Computer Vision*, pages 18312–18321, 2023. 3
- [9] Kangle Deng, Andrew Liu, Jun-Yan Zhu, and Deva Ramanan. Depth-supervised nerf: Fewer views and faster training for free. *arXiv preprint arXiv:2107.02791*, 2021. 2, 3
- [10] Yang Fu, Sifei Liu, Amey Kulkarni, Jan Kautz, Alexei A Efros, and Xiaolong Wang. Colmap-free 3d gaussian splatting. *arXiv preprint arXiv:2312.07504*, 2023. 2, 3, 6, 7, 9, 10
- [11] Ajay Jain, Matthew Tancik, and Pieter Abbeel. Putting nerf on a diet: Semantically consistent few-shot view synthesis. In *Proceedings of the IEEE/CVF International Conference on Computer Vision*, pages 5885–5894, 2021. 2
- [12] Yoonwoo Jeong, Seokjun Ahn, Christopher Choy, Anima Anandkumar, Minsu Cho, and Jaesik Park. Self-calibrating neural radiance fields. In *Proceedings of the IEEE/CVF International Conference on Computer Vision*, pages 5846–5854, 2021. 3
- [13] Bernhard Kerbl, Georgios Kopanas, Thomas Leimkühler, and George Drettakis. 3d gaussian splatting for real-time radiance field rendering. *ACM Transactions on Graphics (TOG)*, 42(4):1–14, 2023. 2, 3, 5, 7
- [14] Arno Knapitsch, Jaesik Park, Qian-Yi Zhou, and Vladlen Koltun. Tanks and temples: Benchmarking large-scale scene reconstruction. *ACM Transactions on Graphics (TOG)*, 36(4):1–13, 2017. 2, 6
- [15] Yixing Lao, Xiaogang Xu, Xihui Liu, Hengshuang Zhao, et al. Corresnerf: Image correspondence priors for neural radiance fields. *Advances in Neural Information Processing Systems*, 36, 2024. 3
- [16] Chen-Hsuan Lin, Wei-Chiu Ma, Antonio Torralba, and Simon Lucey. Barf: Bundle-adjusting neural radiance fields. In *Proceedings of the IEEE/CVF International Conference on Computer Vision*, pages 5741–5751, 2021. 3
- [17] Andreas Meuleman, Yu-Lun Liu, Chen Gao, Jia-Bin Huang, Changil Kim, Min H Kim, and Johannes Kopf. Progressively optimized local radiance fields for robust view synthesis. In *Proceedings of the IEEE/CVF Conference on Computer Vision and Pattern Recognition*, pages 16539–16548, 2023. 3
- [18] Ben Mildenhall, Pratul P Srinivasan, Rodrigo Ortiz-Cayon, Nima Khademi Kalantari, Ravi Ramamoorthi, Ren Ng, and Abhishek Kar. Local light field fusion: Practical view synthesis with prescriptive sampling guidelines. *ACM Transactions on Graphics (TOG)*, 38(4):1–14, 2019. 2

- [19] Ben Mildenhall, Pratul P Srinivasan, Matthew Tancik, Jonathan T Barron, Ravi Ramamoorthi, and Ren Ng. Nerf: Representing Scenes As Neural Radiance Fields for View Synthesis. *Communications of the ACM*, 65(1):99–106, 2021. 2, 5
- [20] Michael Niemeyer, Jonathan T Barron, Ben Mildenhall, Mehdi SM Sajjadi, Andreas Geiger, and Noha Radwan. Regnerf: Regularizing neural radiance fields for view synthesis from sparse inputs. *arXiv preprint arXiv:2112.00724*, 2021. 2
- [21] Eric Penner and Li Zhang. Soft 3D Reconstruction for View Synthesis. *ACM Transactions on Graphics (TOG)*, 36(6):1–11, 2017. 2
- [22] F Plastria. The weiszfeld algorithm: proof, amendments and extensions, ha eiselt and v. marianov (eds.) foundations of location analysis, international series in operations research and management science, 2011. 4
- [23] Alec Radford, Jong Wook Kim, Chris Hallacy, Aditya Ramesh, Gabriel Goh, Sandhini Agarwal, Girish Sastry, Amanda Askell, Pamela Mishkin, Jack Clark, et al. Learning transferable visual models from natural language supervision. In *International Conference on Machine Learning*, pages 8748–8763. PMLR, 2021. 2
- [24] Johannes L Schonberger and Jan-Michael Frahm. Structure-from-motion revisited. In *Proceedings of the IEEE conference on computer vision and pattern recognition*, pages 4104–4113, 2016. 2
- [25] Steven M Seitz and Charles R Dyer. Photorealistic Scene Reconstruction by Voxel Coloring, 2002. US Patent 6,363,170. 2
- [26] Pratul P Srinivasan, Richard Tucker, Jonathan T Barron, Ravi Ramamoorthi, Ren Ng, and Noah Snavely. Pushing the Boundaries of View Extrapolation With Multiplane Images. In *Proceedings of the IEEE/CVF Conference on Computer Vision and Pattern Recognition*, pages 175–184, 2019.
- [27] Pratul P Srinivasan, Ben Mildenhall, Matthew Tancik, Jonathan T Barron, Richard Tucker, and Noah Snavely. Lighthouse: Predicting Lighting Volumes for Spatially-Coherent Illumination. In *Proceedings of the IEEE/CVF Conference on Computer Vision and Pattern Recognition*, pages 8080–8089, 2020. 2
- [28] Prune Truong, Marie-Julie Rakotosaona, Fabian Manhardt, and Federico Tombari. Sparf: Neural radiance fields from sparse and noisy poses. In *Proceedings of the IEEE/CVF Conference on Computer Vision and Pattern Recognition*, pages 4190–4200, 2023. 3
- [29] Shinji Umeyama. Least-squares estimation of transformation parameters between two point patterns. *IEEE Transactions on Pattern Analysis & Machine Intelligence*, 13(04): 376–380, 1991. 6
- [30] Guangcong Wang, Zhaoxi Chen, Chen Change Loy, and Ziwei Liu. Sparsenerf: Distilling depth ranking for few-shot novel view synthesis. *arXiv preprint arXiv:2303.16196*, 2023. 2, 3
- [31] Shuzhe Wang, Vincent Leroy, Johann Cabon, Boris Chidlovskii, and Jerome Revaud. Dust3r: Geometric 3d vision made easy. *arXiv preprint arXiv:2312.14132*, 2023. 2, 3, 4, 7
- [32] Zhou Wang, Alan C Bovik, Hamid R Sheikh, and Eero P Simoncelli. Image quality assessment: from error visibility to structural similarity. *IEEE transactions on image processing*, 13(4):600–612, 2004. 6
- [33] Zirui Wang, Shangzhe Wu, Weidi Xie, Min Chen, and Victor Adrian Prisacariu. Nerf-: Neural radiance fields without known camera parameters. *arXiv preprint arXiv:2102.07064*, 2021. 3, 5, 6, 7, 9
- [34] Rundi Wu, Ben Mildenhall, Philipp Henzler, Keunhong Park, Ruiqi Gao, Daniel Watson, Pratul P Srinivasan, Dor Verbin, Jonathan T Barron, Ben Poole, et al. Reconfusion: 3d reconstruction with diffusion priors. *arXiv preprint arXiv:2312.02981*, 2023. 2
- [35] Haolin Xiong, Sairisheek Muttukuru, Rishi Upadhyay, Pradyumna Chari, and Achuta Kadambi. Sparseggs: Real-time 360 $\{\deg\}$ sparse view synthesis using gaussian splatting. *arXiv preprint arXiv:2312.00206*, 2023. 2, 3
- [36] Dejia Xu, Yifan Jiang, Peihao Wang, Zhiwen Fan, Humphrey Shi, and Zhangyang Wang. Sinnerf: Training neural radiance fields on complex scenes from a single image. In *European Conference on Computer Vision*, pages 736–753. Springer, 2022. 2
- [37] Qiangeng Xu, Zexiang Xu, Julien Philip, Sai Bi, Zhixin Shu, Kalyan Sunkavalli, and Ulrich Neumann. Pointnerf: Point-based neural radiance fields. In *Proceedings of the IEEE/CVF conference on computer vision and pattern recognition*, pages 5438–5448, 2022. 2
- [38] Jiawei Yang, Marco Pavone, and Yue Wang. Freenerf: Improving few-shot neural rendering with free frequency regularization. In *Proceedings of the IEEE/CVF Conference on Computer Vision and Pattern Recognition*, pages 8254–8263, 2023. 2
- [39] Alex Yu, Vickie Ye, Matthew Tancik, and Angjoo Kanazawa. pixelnerf: Neural radiance fields from one or few images. In *Proceedings of the IEEE/CVF Conference on Computer Vision and Pattern Recognition*, pages 4578–4587, 2021. 2
- [40] Xianggang Yu, Mutian Xu, Yidan Zhang, Haolin Liu, Chongjie Ye, Yushuang Wu, Zizheng Yan, Chenming Zhu, Zhangyang Xiong, Tianyou Liang, et al. Mvimgnet: A large-scale dataset of multi-view images. In *Proceedings of the IEEE/CVF conference on computer vision and pattern recognition*, pages 9150–9161, 2023. 2, 6
- [41] Richard Zhang, Phillip Isola, Alexei A Efros, Eli Shechtman, and Oliver Wang. The unreasonable effectiveness of deep features as a perceptual metric. In *Proceedings of the IEEE conference on computer vision and pattern recognition*, pages 586–595, 2018. 6
- [42] Zehao Zhu, Zhiwen Fan, Yifan Jiang, and Zhangyang Wang. Fsgs: Real-time few-shot view synthesis using gaussian splatting. *arXiv preprint arXiv:2312.00451*, 2023. 2, 3, 6
- [43] Matthias Zwicker, Hanspeter Pfister, Jeroen Van Baar, and Markus Gross. Ewa volume splatting. In *Proceedings Visualization, 2001. VIS'01.*, pages 29–538. IEEE, 2001. 2